Modeling of temperature field and solidified surface profile during gas–metal arc fillet welding

C.-H. Kim, W. Zhang, and T. DebRoy[a)]
Department of Materials Science and Engineering, Pennsylvania State University, University Park, Pennsylvania 16802

(Received 24 March 2003; accepted 22 May 2003)

The temperature profiles, weld pool shape and size, and the nature of the solidified weld pool reinforcement surface during gas–metal arc (GMA) welding of fillet joints were studied using a three-dimensional numerical heat transfer model. The model solves the energy conservation equation using a boundary fitted coordinate system. The weld pool surface profile was calculated by minimizing the total surface energy. Apart from the direct transport of heat from the welding arc, additional heat from the metal droplets was modeled considering a volumetric heat source. The calculated shape and size of the fusion zone, finger penetration characteristic of the GMA welds, and the solidified free surface profile were in fair agreement with the experimental results for various welding conditions. In particular, the computed values of important geometric parameters of fillet welds, i.e., the leg length, the penetration depth, and the actual throat, agreed well with those measured experimentally for various heat inputs. The weld thermal cycles and the cooling rates were also in good agreement with independent experimental data. © *2003 American Institute of Physics.*
[DOI: 10.1063/1.1592012]

I. INTRODUCTION

In recent years, numerical calculations of heat transfer, fluid flow, and mass transfer have provided significant insight about the fusion welding processes and welded materials that could not have been achieved otherwise.[1–3] The ability to accurately calculate temperature and velocity fields and thermal cycles has enabled quantitative probing of the size and shape of the fusion zone and, in many cases, the heat affected zone (HAZ). Numerical models have been used to understand various weldment characteristics for a wide variety of welding conditions in materials with diverse thermophysical properties.[4–17] Examples include quantitative understanding of weld temperature and velocity fields,[4–7] phase composition,[8–10] grain structure,[10,11] inclusion structure,[12–14] weld metal composition change owing to both evaporation of alloying elements[15,16] and dissolution of gases.[17]

Previous computer simulation efforts to understand welding processes and welded materials through numerical heat transfer calculations have focused mainly on simple systems. Most of the studies considered butt welding of a rectangular workpiece and ignored any deformation of the weld pool top surface. During fusion welding, many physical processes occur simultaneously. For example, in gas–metal arc (GMA) welding, heat is transported from the arc to the workpiece and the liquid metal droplets formed from the electrode wire also carry heat and mass into the weld pool. Depending on the current and the voltage, the arc can exert significant pressure on the surface of the weld pool. The deformation of the weld pool surface can affect heat transfer and the eventual solidified surface profile of the weld bead. The welding parameters affect droplet diameter, transfer frequency, acceleration, impingement velocity, and the arc length. All of these parameters, in turn, affect the resulting temperature field, thermal cycles, and the structure and properties of the weldment. In fillet welding, the complexity of the welding process is often augmented by the complicated joint geometry containing a curved weld pool surface. All of these complexities must be taken into account to accurately model heat transfer.

A fundamental understanding of heat transfer and fluid flow considering free surface deformation is still evolving. Fusion welding of butt joints with free surface deformation has been studied by Wu and Dorn[5] and Kim and Na.[18] Fan and Kovacevic[19] studied the metal droplet transfer during GMA welding using a model based on the volume of fluid method for two-dimensional spot welding. Kumar and Bhaduri[20] used a finite element model with a volumetric heat source to simulate the heat transfer from metal droplets during GMA welding assuming a flat weld pool surface. Jeong and Cho[21] analytically calculated transient temperature distribution in the fillet welds assuming a flat bead surface. Cho and Kim[22] studied the thermal history using a two-dimensional finite element analysis considering the bead shape for the horizontal fillet joints. Due to the complexity of GMA fillet welding processes, a three-dimensional (3D) framework for weld bead shape control based on scientific principles still remains to be undertaken. With the advancement of computational hardware and software, it has now become practical to relax some of the simplifying assumptions of the previous research and address more realistic situations.

Realistic simulation of GMA fillet welding needs to include several special features. These include complex weldment geometry, the significant deformation of the weld pool top surface, and filler metal addition that are difficult to rep-

a)Electronic mail: debroy@psu.edu

resent adequately by orthogonal rectangular grids. Boundary fitted deformable grids require special transformation of the governing equations and the boundary conditions. The transport of the metal drops into the weld pool is largely responsible for the finger penetration commonly observed in the fusion zone. Thus, the model must take into account the detailed knowledge base of how the droplet size, acceleration, impingement velocity, and arc length affect heat transfer.

GMA fillet welding was studied using a boundary fitted coordinate system to accurately calculate the temperature field in the complex physical domain considering deformation of the weld pool surface. The energy conservation equation and corresponding boundary conditions were transformed into the curvilinear coordinate system. The additional heat from the metal droplets was modeled considering the available knowledge base of the interaction between metal droplets and the weld pool for various welding conditions. The transformed equations were discretized and solved in a simple rectangular computational domain. The free surface profile was calculated by minimizing the total free surface energy considering the addition of filler metal. The model was used to quantitatively understand the effect of welding parameters on the weld bead geometry and cooling rates. In particular, the calculated fusion zone shape and size, finger penetration, and cooling rates were compared with the corresponding experimental results for various welding conditions.

II. MATHEMATICAL FORMULATION

A. Assumptions and salient features

Because of the complexity of the GMA fillet welding, the following simplifying assumptions were made to make the computational work tractable. (a) Two main thermophysical properties needed for the calculations, i.e., the thermal diffusivity and the specific heat for the workpiece material A-36 steel, are not readily available for the temperature range of interest. Therefore, constant values of these parameters were used in the calculations. The model is capable of easily incorporating temperature dependent thermophysical properties. (b) The effect of fluid flow in the weld pool was taken into account through the use of an enhanced thermal conductivity which is widely used in numerical heat transfer in welding. (c) The heat transported by the droplets was taken into account using a time-averaged volumetric heat source which has been widely used in literature. (d) The heat flux from the arc was assumed to have a Gaussian distribution. (e) The available experimental data in literature[23] showed that under the welding conditions considered in this research, the droplet temperature was roughly 2673 K.

The model takes into account the complex joint geometry of the fillet welds, the deformation of the weld pool surface, additions of the filler metal, and the detailed calculations of the heat transfer by the droplets. The output from the model includes temperature field, thermal cycles, fusion zone geometry, and the solidified geometry of the weld reinforcement.

B. Equation of conservation of energy in the curvilinear coordinate system

By using a coordinate system attached with the heat source, the following energy conservation equation can be written in the Cartesian coordinate system:[4,24]

$$\nabla\cdot(\alpha\nabla h)-\rho U_w\frac{\partial h}{\partial x}-\rho U_w L\frac{\partial f_l}{\partial x}+S_v=0, \tag{1}$$

where ρ is the density, h is the sensible heat, α is the thermal diffusion coefficient ($\alpha=k/C_p$, where k is the thermal conductivity and C_p is the specific heat), L is the latent heat of fusion, f_l is the liquid fraction, U_w is the welding speed, and S_v is the power density of a volumetric heat source that represents the additional heat from the metal droplets. The calculation of S_v is discussed in Sec. II C. The sensible heat h is expressed as $h=\int C_p dT$, where T is the temperature. The liquid fraction f_l is assumed to vary linearly with temperature for simplicity:

$$f_l=\begin{cases}1 & T\geqslant T_l\\ \dfrac{T-T_s}{T_l-T_s} & T_s<T<T_l,\\ 0 & T\leqslant T_s\end{cases} \tag{2}$$

where T_l and T_s are the liquidus and solidus temperatures, respectively. Accurate calculation of heat transfer with a deformable weld pool surface requires the use of a nonorthogonal deformable grid to fit the surface profile. Therefore, the energy conservation equation was transformed from the Cartesian to curvilinear coordinate system, as discussed in the following section.

1. Coordinate transformation

In the following discussion, the physical space is denoted by (x,y,z), and the computational domain is represented by (ξ,η,ζ). For clarity, subscripts x, y, z, ξ, η, and ζ are used to represent corresponding partial derivatives. For example, symbols ξ_x and h_η represent the partial derivatives $\partial\xi/\partial x$ and $\partial h/\partial\eta$, respectively. Figure 1 shows the transformation from the L-shaped physical domain to a simple rectangular computational domain. Only the z direction in the physical domain is transformed into the ζ direction in the computational domain, while the ξ and η directions remain the same as the x and y directions, respectively. As shown in Appendix A, the transformed energy conservation equation in the curvilinear coordinate system is given as

$$\begin{aligned}&\frac{\partial}{\partial\xi}\left[\alpha\left(\frac{1}{J}\frac{\partial h}{\partial\xi}+q_{13}\frac{\partial h}{\partial\zeta}\right)\right]+\frac{\partial}{\partial\eta}\left[\alpha\left(\frac{1}{J}\frac{\partial h}{\partial\eta}+q_{23}\frac{\partial h}{\partial\zeta}\right)\right]\\&\quad+\frac{\partial}{\partial\zeta}\left[\alpha\left(q_{31}\frac{\partial h}{\partial\xi}+q_{32}\frac{\partial h}{\partial\eta}+q_{33}\frac{\partial h}{\partial\zeta}\right)\right]-\rho U_w\left[\frac{\partial}{\partial\xi}\left(\frac{h}{J}\right)\right.\\&\quad\left.+\frac{\partial(q_{13}h)}{\partial\zeta}\right]-\rho U_w L\left[\frac{\partial}{\partial\xi}\left(\frac{f_l}{J}\right)+\frac{\partial(q_{13}f_l)}{\partial\zeta}\right]+\frac{S_v}{J}=0,\end{aligned} \tag{3}$$

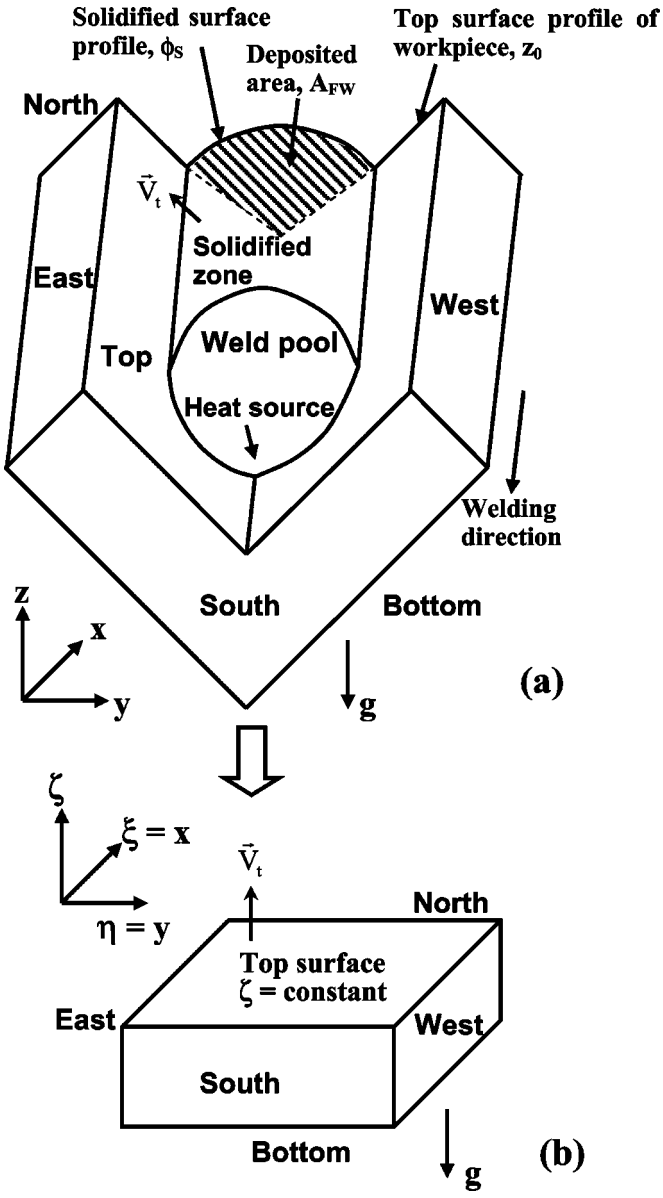

FIG. 1. Schematic plot showing the coordinate transformation from the physical (x,y,z) to the computational domain (ξ, η, ζ), where the transformed energy conservation equation is numerically solved: (a) physical domain and (b) computational domain. Symbol $\mathbf{V}_t$ is a normal vector to the top surface. The shadowed area, A_{FW}, is equal to the amount of fed wire per unit length.

where J is the Jacobian of the transformation given as $J = 1/z_\zeta = 1/(\partial z/\partial\zeta)$, and the coefficients q_{13} to q_{33} are defined as

$$q_{13}=q_{31}=-z_\xi=-\frac{\partial z}{\partial\xi},$$

$$q_{23}=q_{32}=-z_\eta=-\frac{\partial z}{\partial\eta}, \tag{4}$$

$$q_{33}=J(z_\xi^2+z_\eta^2+1)=J\left(\left(\frac{\partial z}{\partial\xi}\right)^2+\left(\frac{\partial z}{\partial\eta}\right)^2+1\right).$$

2. Boundary conditions

As shown in Fig. 1(a), the heat flux at the top surface, F_t, is given as[10,24]

$$\alpha\nabla h\cdot\mathbf{n}_t=F_t=\frac{IV\eta}{2\pi r_b^2}\exp\left(-\frac{x_h^2+y_h^2}{2r_b^2}\right)(\mathbf{k}\cdot\mathbf{n}_t) - \sigma\varepsilon(T^4-T_a^4)-h_c(T-T_a), \tag{5}$$

where $\mathbf{k}$ is a unit in the z direction, $\mathbf{n}_t$ is a unit normal vector to the top surface, I is the current, V is the voltage, η is the arc efficiency (a value of 54% is used), r_b is the heat distribution parameter, x_h and y_h are the x and y distances to the arc axis, respectively, σ is the Stefan–Boltzmann constant, ε is the emissivity, h_c is the convective heat transfer coefficient, and T_a is the ambient temperature (a value of 298 K is used). In Eq. (5), the first term on the right-hand side is the heat input from the arc defined by a Gaussian heat distribution. The second and third terms represent the heat loss by radiation and convection, respectively. Since the radiation heat loss represents only a very small fraction of the net heat flux at the top surface, the effect of geometry on radiation is neglected, i.e., the view factor for two perpendicular steel plates is assumed to be unity for simplicity. As shown in Fig. 1(b), the top surface is defined as $\zeta=$constant. Therefore, Eq. (5) is transformed into the following equation in the curvilinear coordinate:

$$\left.\frac{\partial h}{\partial\zeta}\right|_t=\frac{\dfrac{F_t\|\mathbf{V}_t\|}{J\alpha}+\dfrac{\partial h}{\partial\xi}z_\xi+\dfrac{\partial h}{\partial\eta}z_\eta}{J(z_\xi^2+z_\eta^2+1)}, \tag{6}$$

where $\mathbf{V}_t$ is a normal vector to the top surface defined as $\partial\zeta/\partial x\mathbf{i}+\partial\zeta/\partial y\mathbf{j}+\partial\zeta/\partial z\mathbf{k}$,[25] and $\|\mathbf{V}_t\|$ is its norm. For the bottom surface, the heat flux, F_B, is given as

$$\alpha\nabla h\cdot\mathbf{n}_b=F_b=h_c(T-T_a), \tag{7}$$

where $\mathbf{n}_b$ is a unit normal vector to the bottom surface. Similar to the heat flux equation at the top surface, Eq. (7) is transformed to the following expression in the curvilinear coordinate:

$$\left.\frac{\partial h}{\partial\zeta}\right|_b=\frac{\dfrac{F_b\|\mathbf{V}_b\|}{J\alpha}+\dfrac{\partial h}{\partial\xi}z_\xi+\dfrac{\partial h}{\partial\eta}z_\eta}{J(z_\xi^2+z_\eta^2+1)}, \tag{8}$$

where $\|\mathbf{V}_b\|$ is the norm of a normal vector to the bottom surface. The temperatures at other surfaces, i.e., east, west, south, and north surfaces are set to the ambient temperature.

C. Droplet heat transfer

The hot molten metal droplets impinge into the weld pool with high velocity and carry heat into the liquid metal pool. The sensible heat of the metal droplets are largely responsible for the formation of finger penetration in the weld pool.[20,24,26,27] The heat transfer from the metal droplets was simulated by considering a cylindrical heat source[20,26] with a time-averaged uniform power density (S_v) in Eq. (1). It should be recognized that the use of a cylindrical volumetric heat source assumes the spray transfer mode, which is consistent with the welding conditions used in the present study.

Three parameters are required to calculate S_v: The radius of the heat source, its effective height, and the total sensible heat input by the droplets. The radius of the volumetric heat source is assumed to be twice as the droplet radius, and the effective height, d, is calculated from the following equation based on energy balance:[20,26]

$$d = h_v - x_v + D_d, \tag{9}$$

where h_v is the estimated height of cavity by the impact of metal droplets, x_v is the distance traveled by the center of the slug between the impingement of two successive droplets, and D_d is the droplet diameter. The total sensible heat input from the metal droplets, Q_d, is given as[6]

$$Q_d = \rho_w \pi r_w^2 w_f C_p (T_d - T_l), \tag{10}$$

where ρ_w is the density of the electrode wire, r_w is the radius of the wire, w_f is the wire feeding rate, T_d is the droplet temperature, and T_l is the liquidus temperature.

The values of h_v and x_v in Eq. (9) are calculated based on energy balance as[20,26]

$$h_v = \left(-\frac{2\gamma}{D_d \rho g} + \sqrt{\left[\left(\frac{2\gamma}{D_d \rho g} \right)^2 + \frac{D_d v_d^2}{6g} \right]} \right), \tag{11}$$

$$x_v = \left(h_V + \frac{2\gamma}{D_d \rho g} \right) \left\{ 1 - \cos\left[\left(\frac{g}{h_v} \right)^{1/2} \Delta t \right] \right\}, \tag{12}$$

where γ is the surface tension of the molten metal ($\mathrm{N\,m^{-1}}$), ρ is the density, g is the gravitational constant, v_d is the droplet impingement velocity, and Δt is the interval between two successive drops ($t = 1/f$, where f is the droplet transfer frequency). As shown in Eqs. (11) and (12), calculation of the dimensions of the volumetric heat source requires the knowledge of the droplet transfer frequency, radius, and impingement velocity. These parameters are determined from the knowledge base available in literature for given welding conditions. The calculation procedure is given in Appendix B. From the computed values of Q_d, D_d, and d, the time-averaged power density of the volumetric heat source, S_v, is calculated as follows:

$$S_v = \frac{Q_d}{\pi D_d^2 d}. \tag{13}$$

It should be noted that Eq. (13) is only valid for grid points within the cylindrical heat source, and the power density is zero outside the cylinder.

D. Weld pool free surface profile

The weld pool free surface profile is determined by minimizing the total surface energy, which includes surface tension energy, the potential energy owing to gravity, and the work performed by the arc force displacing the weld pool surface. The governing equation for the free surface profile is given by[5,18,24]

$$\gamma \left\{ \frac{(1+\phi_y^2)\phi_{xx} - 2\phi_x \phi_y \phi_{xy} + (1+\phi_x^2)\phi_{yy}}{(1+\phi_x^2+\phi_y^2)^{3/2}} \right\} = \rho g \phi + P_a + \lambda, \tag{14}$$

where P_a is the arc pressure and λ is the Lagrange multiplier. The free surface profile, ϕ, is defined as the vertical (z direction) elevation of the top surface with respect to an arbitrarily chosen horizontal plane. The subscripts x and y represent partial derivatives over x and y, respectively. The arc pressure is expressed as[28,29]

$$P_a = \frac{F}{2\pi\sigma_p^2} \exp\left(-\frac{x^2+y^2}{2\sigma_p^2} \right), \tag{15}$$

where F is the total arc force and σ_p is the pressure distribution parameter. The values of F and σ_p were calculated based on the extensive experimental work of Lin and Eagar.[28] As shown in Appendix C, the values of these two parameters could be described as

$$F = -0.040\,17 + 0.000\,255\,3 \times I \quad (\mathrm{N}), \tag{16}$$

$$\sigma_p = 1.4875 + 0.001\,23 \times I \quad (\mathrm{mm}), \tag{17}$$

where I is the welding current in Ampere.

The boundary conditions for the free surface equation are given as

$$\text{At the front pool boundary: } \phi = z_0, \tag{18a}$$

$$\text{At the rear pool boundary: } \frac{\partial \phi}{\partial x} = 0. \tag{18b}$$

Here, the front and rear pool boundaries are defined so that the temperature gradient along the x direction (dT/dx) is positive at the front pool boundary and negative at the rear boundary. As shown in Fig. 1(a), the deposited area, A_{FW}, at a solidified cross section of the fillet weld is equal to the amount of fed wire per unit length[24]

$$\int (\phi_s - z_0)\,dy - \frac{\pi r_w^2 w_f}{U_w} = 0, \tag{19}$$

where ϕ_s is the solidified surface profile, z_0 is the z location of the workpiece top surface, and r_w, w_f, and U_W are the wire radius, wire feeding rate, and the welding speed, respectively.

Calculation of the free surface profile requires the simultaneous solutions of both the free surface Eq. (14) and the constraint Eq. (19). Equation (14) is discretized using the finite difference method and then solved using the Gauss–Seidel point-by-point method[30] for an assumed λ. The resulting free surface profile is applied to the constraint Eq. (19) and the residual [defined as the left-hand side of Eq. (19)] is evaluated. The value of λ is determined iteratively until both Eqs. (14) and (19) are satisfied.

E. Discretization and solution of the governing equations

Figures 2(a) and 2(b) show transformation of a yz plane from the complex physical domain to the simple computational domain. The computational domain is divided into small rectangular control volumes as shown in Figs. 2(c) and 2(d). A grid point is located at the center of each control volume, storing the values of variables such as the sensible heat.

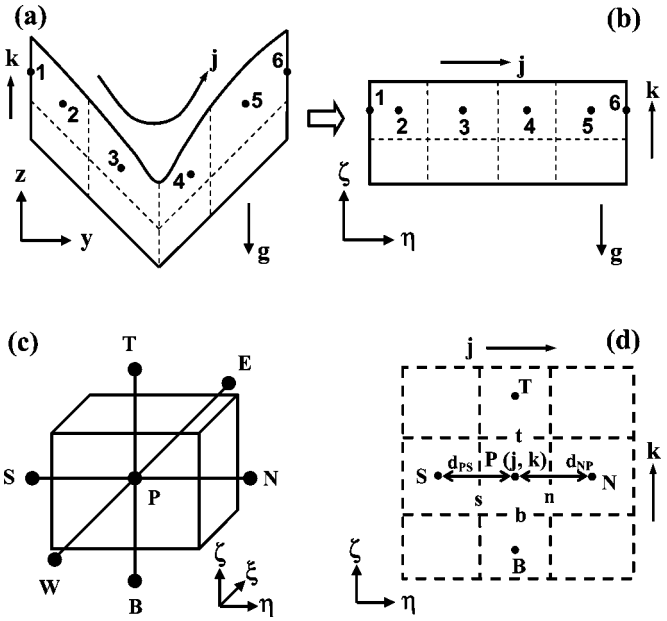

FIG. 2. Grid system in the physical and computational domains: (a) A yz plane in the physical domain, (b) the corresponding $\eta\zeta$ plane in the computational domain, (c) a control volume and scalar grid points in 3D, and (d) control volumes and grid points in a $\eta\zeta$ plane. The dashed lines represent control interfaces of the volume, while the solid dots correspond to grid points. Symbols W, E, S, N, B, and T are the east, west, south, north, bottom, and top neighbors of the grid point P, respectively, while symbols s, n, b, and t are the south, north, bottom, and top interfaces of the control volume P.

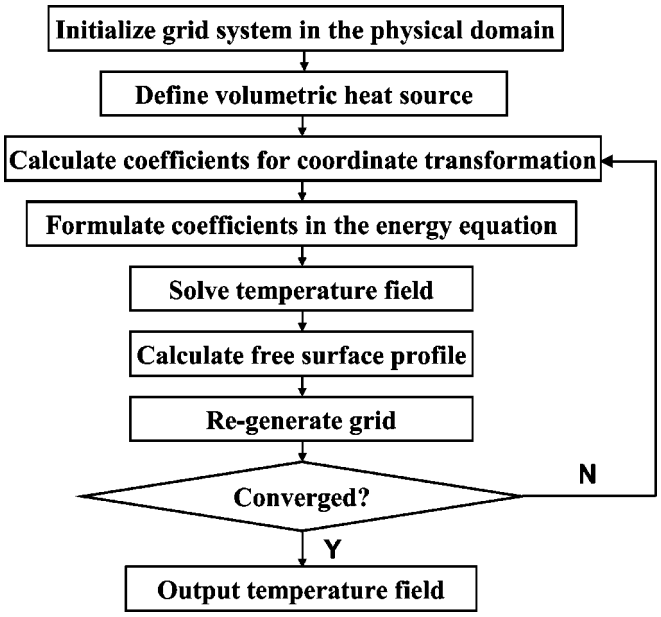

FIG. 3. Schematic diagram showing the overall procedure for the calculation of temperature field and surface profile during GMA fillet welding.

The transformed energy conservation equation in the curvilinear coordinate, i.e., Eq. (3), is discretized using the control volume method.[30] Discretized equations are formulated by integrating the energy conservation equation over the control volumes. For example, for the grid point P shown in Fig. 2(d), the diffusion term $\partial/\partial\eta(\alpha/J\partial h/\partial\eta)$ in Eq. (3) is discretized by integrating this term over the control volume P

$$\int_V\int\int\frac{\partial}{\partial\eta}\left(\frac{\alpha}{J}\frac{\partial h}{\partial\eta}\right)d\xi d\eta d\zeta$$

$$=A_{\mathrm{SN}}\left(\frac{\alpha}{J}\frac{\partial h}{\partial\eta}\right)_s^n$$

$$=A_{\mathrm{SN}}\left[\left(\frac{\alpha}{J}\right)_n\left(\frac{h_N-h_P}{d_{NP}}\right)-\left(\frac{\alpha}{J}\right)_s\left(\frac{h_P-h_S}{d_{PS}}\right)\right]$$

$$=\frac{\alpha_n A_{\mathrm{SN}}}{J_n d_{NP}}h_N-A_{\mathrm{SN}}\left[\frac{\alpha_n}{J_n d_{NP}}+\frac{\alpha_s}{J_s d_{PS}}\right]h_P+\frac{\alpha_s A_{\mathrm{SN}}}{J_s d_{PS}}h_S, \tag{20}$$

where A_{SN} is the area of the south/north interface, d_{PS} and d_{NP} are the distances from point P to S and point N to P, respectively, and subscripts s, n, S, and N indicate the position where the value is evaluated in Fig. 2(d). For example, α_n and J_s are the values of the thermal diffusion coefficient at the north interface and the value of Jacobian at the south interface, respectively. The final discretized equation takes the following form:[30]

$$a_P h_P=\left(\sum_{nb}(a_{nb})-S_P\Delta V\right)h_P=\sum_{nb}(a_{nb}h_{nb})+S_C\Delta V, \tag{21}$$

where subscript P represents a given grid point, while subscript nb represents the six neighbors of grid point P, a is the coefficient calculated based on control volume integration, ΔV is the volume of the given control volume, and terms S_C and S_P come from the source term linearization:[30]

$$S=S_C+S_P h_P. \tag{22}$$

The iterative solution procedure is described in a flow chart shown in Fig. 3. The temperature field is solved first and is then used in the calculation of the free surface profile. After the free surface calculation, the z locations of grids are adjusted to fit the surface profile, and the temperature field is recalculated in the grid system. The calculation procedure is repeated until a converged temperature field and free surface profile are obtained.

The following convergence criteria are used for the calculation of temperature field and free surface profile:

$$\frac{\Sigma_{\mathrm{domain}}|(\Sigma_{nb}(a_{nb}h_{nb})+S_C\Delta V)/a_P-h_P|}{\Sigma_{\mathrm{domain}}|h_P|}<10^{-5}, \tag{23}$$

$$\left|\frac{\lambda-\lambda_{T0}}{\lambda}\right|<10^{-6}. \tag{24}$$

The left-hand side of Eq. (23) corresponds to the residual of the discretized energy equation, which indicates the convergence of the energy equation. The left-hand side of Eq. (24) indicates the convergence of the solution of free surface force balance equation. In Eq. (24), the symbols λ and λ_{T0} are the Lagrange multipliers calculated for the present and previous temperature fields, respectively.

A $72\times66\times47$ grid system was used and the corresponding solution domain had dimensions of 450 mm in length,

TABLE I. Welding conditions used in the experiments. Polarity: direct current electrode positive, Joint type: fillet joint, flat position, 90° joint angle, and no root gap, as shown in Fig. 1, Electrode type: AWS E70S-6, 1.32 mm (0.052 inch) diameter solid wire, Base metal: ASTM A-36 mild steel, Shielding gas: Ar–10% CO_2, and Metal droplet transfer mode: Spray transfer mode.

Case No.	(CTWD) (mm)	Wire feeding rate (mm/s)	Travel speed (mm/s)	Voltage (V)	Estimated current (A)
1	22.2	169.3	4.2	31	312.0
2	22.2	211.7	6.4	31	362.0
3	22.2	169.3	6.4	33	312.0
4	22.2	211.7	4.2	33	362.0
5	28.6	169.3	6.4	31	286.8
6	28.6	169.3	4.2	33	286.8
7	28.6	211.7	4.2	31	331.4
8	28.6	211.7	6.4	33	331.4

108 mm in width, and 18 mm in depth. Spatially nonuniform grids with finer grids near the heat source were used for the maximum resolution of variables. The calculations normally converged within 4000 iterations, which took about 6 min in a personal computer with 2.8 GHz Intel P4 central processing unit and 512 Mb PC2700 DDR-SDRAM memory.

III. RESULTS AND DISCUSSION

The model was used for the calculation of the temperature field and surface profile for the eight cases listed in Table I. The experimental conditions are also given in Table I. The material properties for the A-36 steel workpiece used in the calculations are presented in Table II.

A. Droplet heat transfer

An important feature of the GMA welding is the finger penetration which is mainly caused by the transfer of heat from the superheated metal droplets into the weld pool. Previous work in butt welding has shown that the droplet heat transfer can be effectively simulated by incorporating a time-averaged volumetric heat source term in the energy conservation equation. This volumetric heat source is characterized by its radius, height, and power density. The effects of current, voltage, and contact tube-to-workpiece distance (CTWD) on the computed height of the volumetric heat source are shown in Fig. 4(a). As shown in Fig. 4(a), it is observed that the height of the heat source increases with

TABLE II. Physical properties of the mild steel workpiece used in the calculation.[a]

Physical property	Value
Liquidus temperature, T_L (K)	1785.0
Solidus temperature, T_S (K)	1745.0
Density of metal, ρ-(kg m^{-3})	7200
Thermal conductivity of solid, k_S (J m^{-1} · s^{-1} K^{-1})	21.0
Enhanced thermal conductivity of liquid, k_L (J m^{-1} s^{-1} K^{-1})	420.0
Specific heat of solid, C_{PS} (J kg^{-1}K^{-1})	703.4
Specific heat of liquid, C_{PL} (J kg^{-1}K^{-1})	808.1
Surface tension of liquid metal, γ (N m^{-1})	1.2

[a]See Ref. 4.

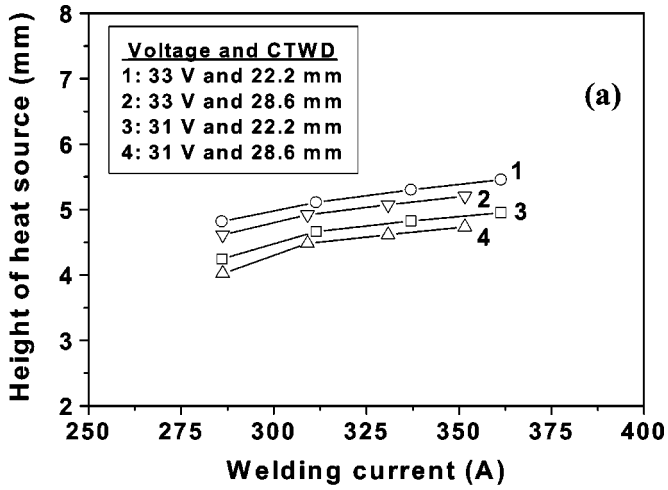

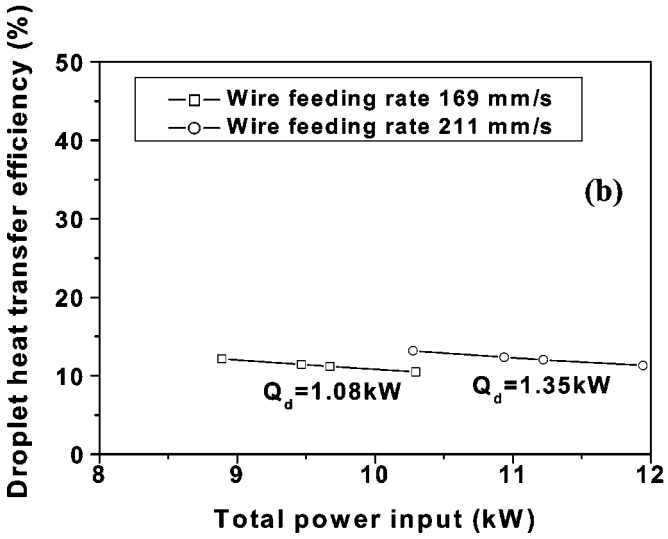

FIG. 4. Calculated parameters of the cylindrical volumetric heat source for various welding conditions: (a) Height of the volumetric heat source and (b) efficiency of droplet heat transfer. The efficiency of the droplet heat transfer is defined as the ratio of the total sensible heat input from metal droplets over the total heat input.

both welding current and voltage, while it decreases with the increase in CTWD. The effect of current can be understood from its effect on the droplet impingement velocity which increases with current. The higher velocity, in turn increases the height of the heat source as can be observed from Eq. (11). When the voltage is increased keeping the current constant, both the arc length and the droplet impingement velocity increase. As a result, the height of the volumetric heat source also increases with voltage. With the increase in CTWD, the impingement velocity decreases which leads to a reduction of the height of the heat source. This is because the increase in CTWD is accompanied by an increase in the wire feeding rate to maintain a target current. As a consequence, the droplet radius increases and the impingement velocity decreases. It will be shown in the next paragraph that the droplets carry a significant amount of energy into the weld pool for the welding conditions investigated. Under these

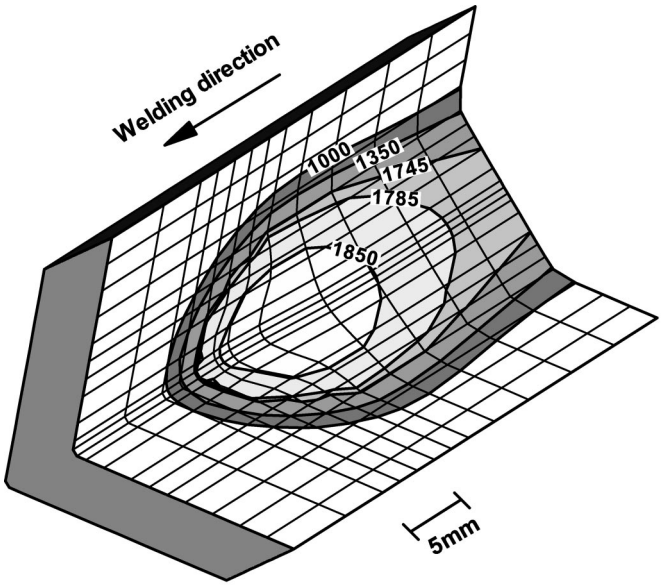

FIG. 5. Calculated temperature field at the weld top surface. The temperatures are given in Kelvin. The thin solid lines represent the deformable grid system used in the calculation. For clarity, only a portion of the workpiece is shown.

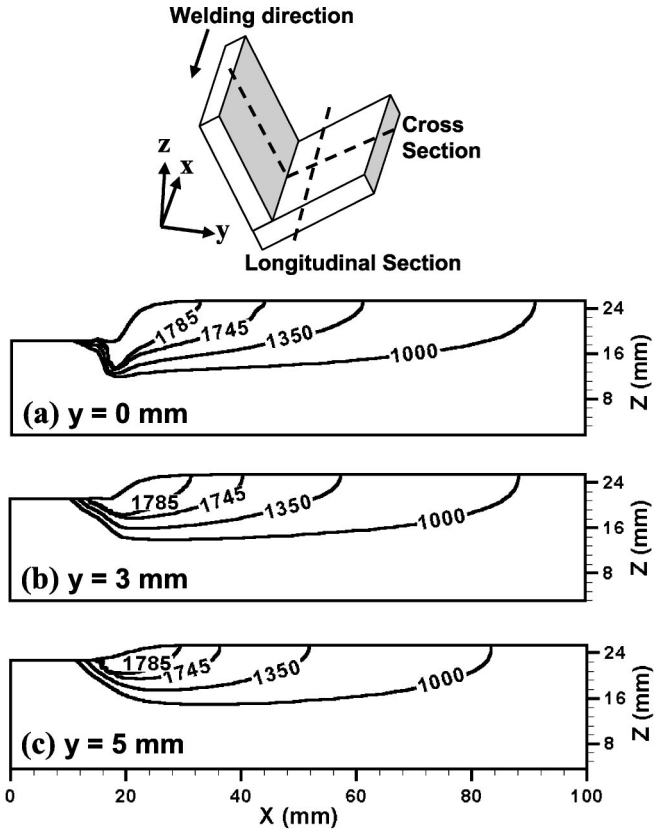

FIG. 6. Calculated temperature fields along various longitudinal sections parallel to the welding direction. The temperatures are given in Kelvin.

conditions, the height of the volumetric heat source significantly affects finger penetration which is a characteristic of the GMA welding.

Figure 4(b) shows the efficiency of droplet heat transfer (η_d), defined as the ratio of the total sensible heat input owing to metal droplets (Q_d) over the total heat input (IV), i.e., $\eta_d = Q_d/(IV)$. Since the droplet temperature does not change significantly for the welding conditions used in this study,[23] the droplet heat transfer rate is determined by the wire feeding rate. Therefore, at a given wire feeding rate, the efficiency of droplet heat transfer is inversely proportional to the total heat input, as shown in Fig. 4(b). The computed values of the efficiency of the droplet heat transfer are found to vary between 10% and 12% for all of the cases studied here. The entire sensible heat of the droplets is distributed to a small cylindrical volume directly under the arc and this distribution of heat is the main reason for the finger penetration observed in the fusion zone of the fillet welds.

B. Temperature distribution in the weldment

The calculated temperature field for case No. 1 (Table I) is shown in Figs. 5 to 7, where the weld pool boundary is represented by the 1745 K solidus isotherm of A-36 steel. As shown in Figs. 5–7, the weld top surface is severely deformed due to the effect of the arc force. The computed results show that the molten metal is pushed to the rear part of the weld pool by the arc force. As a result of the filler metal addition, the solidified weld metal forms pronounced weld reinforcement. Figure 5 shows that the isotherms in front of the weld pool are compressed while those behind the weld pool are expanded because of the motion of the heat source. Figure 5 also indicates that the grid is depressed most pronouncedly under the arc while elevated in the rear part of the weld pool. The effect of the welding speed is apparent from Fig. 6, where the expansion of the isotherms behind the heat source is clearly visible. Figure 6 also shows that the free surface depressed in the weld pool due to the arc force while the solidified region is elevated owing to the filler metal addition. The size of the two-phase mushy zone, de-

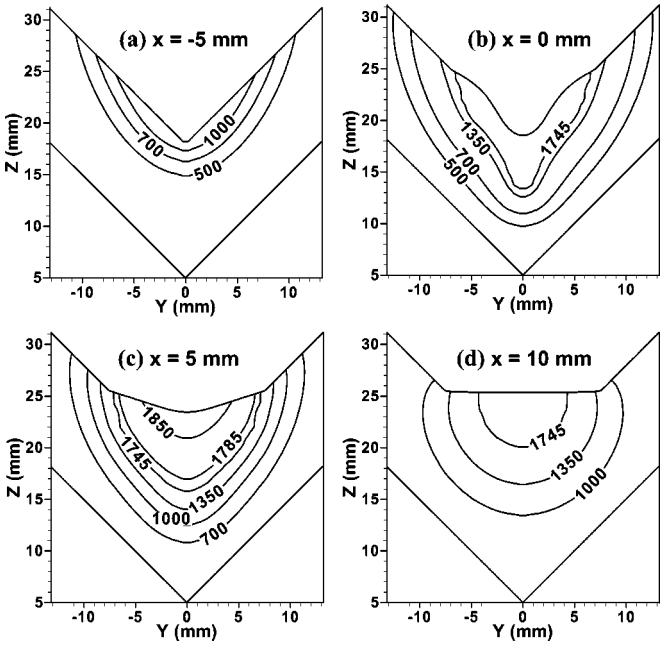

FIG. 7. Calculated temperature field at different cross sections perpendicular to the welding direction. The temperatures are given in Kelvin.

fined by the solidus (1745 K) and the liquidus (1785 K) isotherms is maximum (about 12 mm) at the center plane shown in Fig. 6(a). The mushy zones in planes b and c which are further from the central plane are smaller in size. The temperature profiles in Figs. 6(a) and 7(b) clearly show the finger penetration characteristic of the GMA welding. Figure 7 shows the evolution of the surface profile during welding. As shown in Fig. 7(a), this plane is located 5 mm ahead of the arc, and this region has not yet melted. The region directly under the arc is shown in Fig. 7(b). The depression of the weld pool surface is clearly visible and the temperature profile shows the characteristic shape of finger penetration. As the monitoring location moves away from the arc, the weld pool surface shows considerably less depression as would be expected from the reduction in arc pressure. Furthermore, the accumulation of the liquid metal in the rear of the weld pool is clearly visible in Figs. 7(c) and 7(d). This accumulated metal forms the weld reinforcement after solidification.

The thermal cycles were calculated by converting the x distance into time using the welding speed. Figure 8(a) shows the thermal cycles in the HAZ at the top surface for case No. 1. The heating rate is much steeper than the cooling rate due to the following two reasons. First, the isotherms in front of the arc are compressed while those behind the arc are largely expanded due to the high welding speed. Furthermore, the existence of the volumetric heat source also contributes to the high heating rates. As expected, the peak temperatures are higher at locations close to the weld fusion plane and decrease with distance from this location in the HAZ. The same trend is also observed in the heating and cooling rates.

The average cooling rate, $\dot{T}_{8/5}$, from 1073 K to 773 K (800 °C to 500 °C), which affects the final microstructure of the weld metal,[31] is calculated as

$$\dot{T}_{8/5}=\frac{T_{800}-T_{500}}{t_{8/5}}=\frac{300U_W}{\Delta d}\,\mathrm{K\,s^{-1}}, \tag{25}$$

where $t_{8/5}$ is the cooling time from 1073 K to 773 K, U_W is the welding speed, and Δd is the distance between both points where a line parallel to the x direction intercepts the 1073 K and 773 K isothermal contours. Figure 8(b) shows the calculated average cooling rates at two monitoring locations, i.e., fusion boundary at the top surface and the joint root, for various heat inputs. As shown in Fig. 8(b), the calculated average cooling rate decreases as the heat input per unit length (defined as the total power input/welding speed) increases. Let us consider the changes in cooling rate resulting form an increase in welding speed. As the U_W increases, Δd does not change significantly. As a result, the cooling rate increases. The increase in the welding speed is accompanied by a reduction in the heat input per unit length. Therefore, a reduction in heat input is accompanied by an increase in the cooling rate as observed in Fig. 8(b). On the other hand, when the welding speed is kept constant and the energy input is increased, the isotherms are expanded and the cooling rate will decrease because of higher Δd. Figure 8(b) also shows that the average cooling rates at the joint root are smaller than those at the fusion boundary at the top surface. This is because the heat is conducted more easily at the top surface than at the central plane. Figure 8(b) also indicates that both the calculated average cooling rate and its inverse dependence on the heat input agree reasonably well with those estimated using a cooling rate nomograph available in literature for fillet welds.[31]

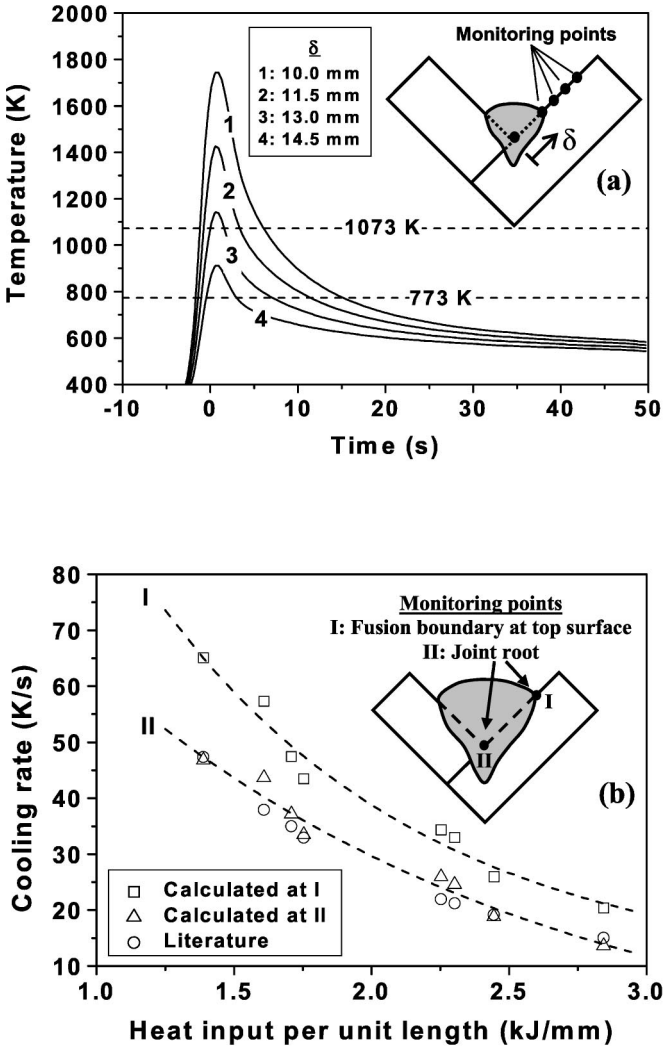

FIG. 8. Calculated temperature distribution in the weldment: (a) Thermal cycles in the HAZ and (b) cooling rates. In (a), symbol δ represents the distance from the joint root to a monitoring location at the top surface. The first monitoring point, i.e., $\delta=10$ mm, is located at the fusion boundary. Time zero is arbitrarily set to be correspondent to $x=0$ mm. In (b), the average cooling rate was calculated using the cooling time from 1073 K to 773 K (800 °C to 500 °C). The two dashed lines are plotted by fitting the calculated cooling rate data at monitoring locations I and II.

C. Fusion zone geometry and the solidified surface profile

The calculated bead shape and temperature fields for all the cases given in Table I are shown in Fig. 9. The calculated fusion zone geometry for all cases agrees reasonably well with the corresponding experimental results. Furthermore, the solidified weld bead shape and the finger penetration could be reasonably predicted by the model. Some discrepancy between the experimental surface profile and the computed results are observed in Figs. 9(c), 9(e), 9(g), and 9(h).

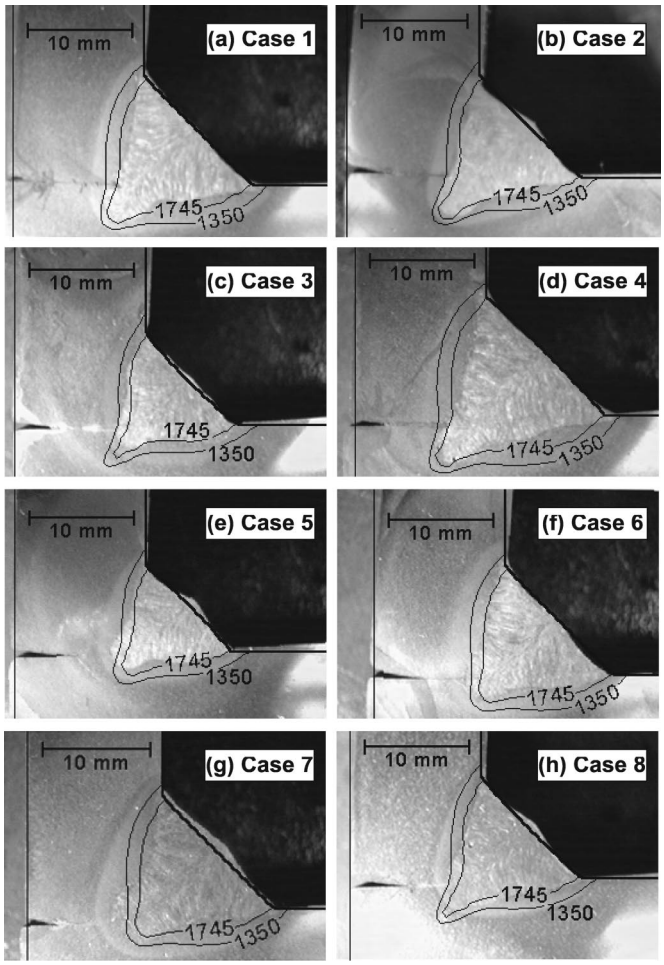

FIG. 9. Comparison between the calculated and experimental weld geometry for different cases given in Table I. Temperatures are given in Kelvin. The 1745 K solidus isotherm corresponds to the calculated weld pool boundary.

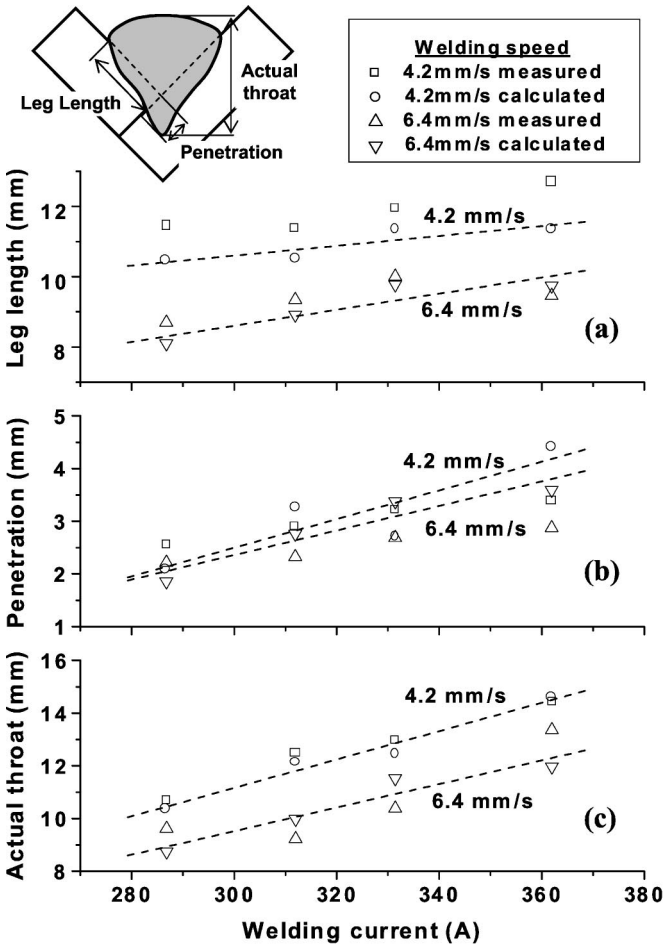

FIG. 10. Weld bead geometric parameters as a function of the current and welding speed: (a) Leg length, (b) penetration, and (c) actual throat. The dashed lines are plotted by fitting the computed data.

Part of this discrepancy is contributed by thermal stress-induced distortion as can be evidenced by the gap between the two plates.

Both the experimental data and the computed results show that three important geometrical parameters of the weld bead, i.e., the leg length, penetration, and the actual throat all increase with the current as can be observed in Fig. 10. Furthermore, the computed results and the experimental data show a reduction in all these dimensions with an increase in the welding speed. It is worth noting that the effect of welding speed is pronounced on the leg length and the actual throat. However, the penetration is not significantly affected by the welding speed. The changes in these geometric parameters, shown in Fig. 10, result from the heat input as well as the dimensions and the power density of the volumetric heat source.

In Fig. 11, these three geometric parameters are also plotted as a function of heat input per unit length. It is observed that only the leg length increases continuously with the increase in heat input. The data for the penetration and actual throat are segregated into clusters with identifiable welding speed. Figures 10 and 11 indicate that the leg length depends strongly on the heat input per unit length while the penetration is affected largely by the welding current. The dependence of the leg length on heat input can be explained from the fact that the heat input per unit length determines the bead cross section and the leg length. On the other hand, the penetration is determined by the dimensions and the power density of the volumetric heat source. Since the actual throat can be approximately determined from a combination of the leg length and penetration based on geometric consideration, the dimensions of the throat cannot be determined solely from the heat input per unit length. The average difference between the calculated and the measured values for the leg length, the actual throat, and penetration were found to be 6%, 6%, and 15%, respectively. These numerical values are to be interpreted with caution because of the limited volume of experimental data and lack of any statistically significant index of the quality of the experimental data. In summary, the trends and values of the geometric variables of the fillet weld could be satisfactorily predicted by the numerical heat transfer model within the range of values of the welding variables investigated.

IV. SUMMARY AND CONCLUSIONS

A 3D numerical heat transfer model was developed to calculate the temperature profiles, weld pool shape and size,

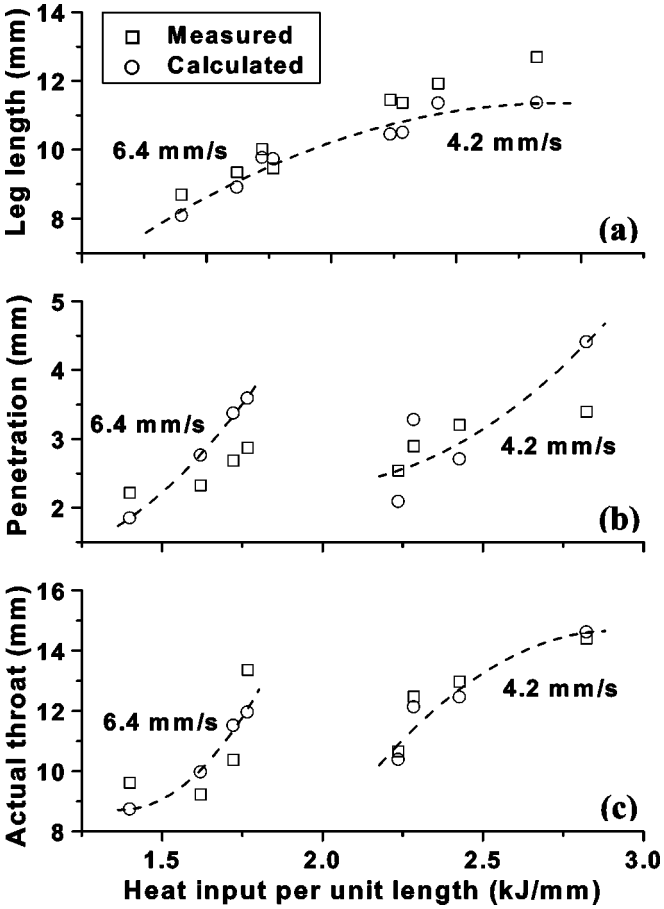

FIG. 11. Weld bead geometric parameters as a function of the heat input per unit length and welding speed: (a) Leg length, (b) penetration, and (c) actual throat. The dashed lines are plotted by fitting the computed results.

and the nature of the solidified weld pool reinforcement surface during GMA welding of fillet joints. The numerical model solves the energy conservation equation in a boundary fitted coordinate system, considering the free surface deformation, filler metal addition, and sensible heat input from the metal droplets. The energy conservation equation and the corresponding boundary conditions were transformed into the curvilinear coordinate system and then solved in a simple rectangular computational domain. This coordinate transformation approach allowed calculation of the temperature field in a complex physical domain containing a deformable free surface.

The numerically computed fusion zone geometry, finger penetration characteristic of the GMA welds, and the solidified surface profile of the weld reinforcement were in fair agreement with the experimental results for various welding conditions. The leg length, penetration, and actual throat were found to increase with the increase in welding current. All of these parameters decreased with the increase in welding speed. The predicted values of these three geometric parameters agreed well with those measured experimentally. Both the experimental results and the model predictions indicated that the average cooling rate between 1073 and 773 K decreased with an increase in heat input per unit length. The weld thermal cycles and the cooling rates were also in good agreement with independent experimental data.

ACKNOWLEDGMENTS

The work was supported by a grant from the U.S. Department of Energy, Office of Basic Energy Sciences, Division of Materials Sciences, under Grant No. DE-FGO2-01ER45900. One of the authors (W.Z.) gratefully acknowledges an award of a Fellowship from the American Welding Society. The authors would like to express their gratitude to Dr. M. A. Quintana of Lincoln Electric Company and Dr. S. S. Babu of Oak Ridge National Laboratory for their interest in the work and for the experimental data. Valuable critical comments from Dr. Amitava De, Yajun Fan, Xiuli He, Amit Kumar, and Saurabh Mishra are appreciated.

APPENDIX

A. Derivation of energy conservation equation in the curvilinear coordinate

The following chain rule[25,32] is applied for the coordinate transformation from the Cartesian (x,y,z) to the curvilinear coordinate (ξ, η, ζ):

$$\frac{\partial}{\partial x}=\frac{\partial}{\partial \xi}\frac{\partial \xi}{\partial x}+\frac{\partial}{\partial \eta}\frac{\partial \eta}{\partial x}+\frac{\partial}{\partial \zeta}\frac{\partial \zeta}{\partial x}=\xi_x\frac{\partial}{\partial \xi}+\eta_x\frac{\partial}{\partial \eta}+\zeta_x\frac{\partial}{\partial \zeta},$$

$$\frac{\partial}{\partial y}=\frac{\partial}{\partial \xi}\frac{\partial \xi}{\partial y}+\frac{\partial}{\partial \eta}\frac{\partial \eta}{\partial y}+\frac{\partial}{\partial \zeta}\frac{\partial \zeta}{\partial y}=\xi_y\frac{\partial}{\partial \xi}+\eta_y\frac{\partial}{\partial \eta}+\zeta_y\frac{\partial}{\partial \zeta}, \tag{A1}$$

$$\frac{\partial}{\partial z}=\frac{\partial}{\partial \xi}\frac{\partial \xi}{\partial z}+\frac{\partial}{\partial \eta}\frac{\partial \eta}{\partial z}+\frac{\partial}{\partial \zeta}\frac{\partial \zeta}{\partial z}=\xi_z\frac{\partial}{\partial \xi}+\eta_z\frac{\partial}{\partial \eta}+\zeta_z\frac{\partial}{\partial \zeta},$$

where the coefficients such as ξ_x and η_y are numerically computed using the following relationship:[25,32]

$$\begin{bmatrix} \xi_x & \xi_y & \xi_z \\ \eta_x & \eta_y & \eta_z \\ \zeta_x & \zeta_y & \zeta_z \end{bmatrix} = J\begin{bmatrix} y_\eta z_\zeta - y_\zeta z_\eta & x_\zeta z_\eta - x_\eta z_\zeta & x_\eta y_\zeta - x_\zeta y_\eta \\ y_\zeta z_\xi - y_\xi z_\zeta & x_\xi z_\zeta - x_\zeta z_\xi & x_\zeta y_\xi - x_\xi y_\zeta \\ y_\xi z_\eta - y_\eta z_\xi & x_\eta z_\xi - x_\xi z_\eta & x_\xi y_\eta - x_\eta y_\xi \end{bmatrix}, \tag{A2}$$

where J is the Jacobian of the coordinate transformation given as

$$J=\frac{\partial(\xi,\eta,\zeta)}{\partial(x,y,z)} = \frac{1}{x_\xi(y_\eta z_\zeta - y_\zeta z_\eta)-x_\eta(y_\xi z_\zeta - y_\zeta z_\xi)+x_\zeta(y_\xi z_\eta - y_\eta z_\xi)}. \tag{A3}$$

Let us first consider transformation of $\partial\phi/\partial xi$, where ϕ is a general variable such as h, and xi is the distance along the ith direction ($xi=x$, y, and z when $i=1$, 2, and 3, respectively). Applying the chain rule, i.e., Eq. (A1), we have

$$\frac{\partial \phi}{\partial xi}=\xi_{xi}\frac{\partial \phi}{\partial \xi}+\eta_{xi}\frac{\partial \phi}{\partial \eta}+\zeta_{xi}\frac{\partial \phi}{\partial \zeta}. \tag{A4}$$

It should be noted that this equation is no longer a conservative form. To recast the equation into a conservative

form, Eq. (A4) is first divided by J, and then a combination of terms which sums up to zero is added, as follows:[32]

$$\frac{1}{J}\frac{\partial\phi}{\partial xi}=\frac{\xi_{xi}}{J}\frac{\partial\phi}{\partial\xi}+\frac{\eta_{xi}}{J}\frac{\partial\phi}{\partial\eta}+\frac{\zeta_{xi}}{J}\frac{\partial\phi}{\partial\zeta}+\left[\phi\frac{\partial}{\partial\xi}\left(\frac{\xi_{xi}}{J}\right)-\phi\frac{\partial}{\partial\xi}\left(\frac{\xi_{xi}}{J}\right)\right]+\left[\phi\frac{\partial}{\partial\eta}\left(\frac{\eta_{xi}}{J}\right)-\phi\frac{\partial}{\partial\eta}\left(\frac{\eta_{xi}}{J}\right)\right]+\left[\phi\frac{\partial}{\partial\zeta}\left(\frac{\zeta_{xi}}{J}\right)-\phi\frac{\partial}{\partial\zeta}\left(\frac{\zeta_{xi}}{J}\right)\right]. \tag{A5}$$

Rearranging Eq. (A5), we have

$$\frac{1}{J}\frac{\partial\phi}{\partial xi}=\frac{\partial}{\partial\xi}\left(\frac{\phi\xi_{xi}}{J}\right)+\frac{\partial}{\partial\eta}\left(\frac{\phi\eta_{xi}}{J}\right)+\frac{\partial}{\partial\zeta}\left(\frac{\phi\zeta_{xi}}{J}\right)-\phi\left[\frac{\partial}{\partial\xi}\left(\frac{\xi_{xi}}{J}\right)+\frac{\partial}{\partial\eta}\left(\frac{\eta_{xi}}{J}\right)+\frac{\partial}{\partial\zeta}\left(\frac{\zeta_{xi}}{J}\right)\right]. \tag{A6}$$

Substituting the relationships shown in Eq. (A2), the term within the square bracket is found to be zero. Therefore, the conservative form of $\partial\phi/\partial xi$ is given as

$$\frac{\partial\phi}{\partial xi}=J\left[\frac{\partial}{\partial\xi}\left(\frac{\phi\xi_{xi}}{J}\right)+\frac{\partial}{\partial\eta}\left(\frac{\phi\eta_{xi}}{J}\right)+\frac{\partial}{\partial\zeta}\left(\frac{\phi\zeta_{xi}}{J}\right)\right]. \tag{A7}$$

Compared with the nonconservative form shown in Eq. (A4), the conservative form is a better numerical representation of the net flux through the volume element[25,32] and, therefore, is normally used.

Applying Eq. (A7), the energy conservation equation in the curvilinear system is formulated as

$$\frac{\partial}{\partial\xi}\left[\frac{\alpha}{J}\left(Q_{11}\frac{\partial h}{\partial\xi}+Q_{12}\frac{\partial h}{\partial\eta}+Q_{13}\frac{\partial h}{\partial\zeta}\right)\right]+\frac{\partial}{\partial\eta}\left[\frac{\alpha}{J}\left(Q_{21}\frac{\partial h}{\partial\xi}+Q_{22}\frac{\partial h}{\partial\eta}+Q_{23}\frac{\partial h}{\partial\zeta}\right)\right]+\frac{\partial}{\partial\zeta}\left[\frac{\alpha}{J}\left(Q_{31}\frac{\partial h}{\partial\xi}+Q_{32}\frac{\partial h}{\partial\eta}+Q_{33}\frac{\partial h}{\partial\zeta}\right)\right]-\rho U_w\left[\frac{\partial}{\partial\xi}\left(\frac{h\xi_x}{J}\right)+\frac{\partial}{\partial\eta}\left(\frac{h\eta_x}{J}\right)+\frac{\partial}{\partial\zeta}\left(\frac{h\zeta_x}{J}\right)\right]-\rho U_w L\left[\frac{\partial}{\partial\xi}\left(\frac{f_l\xi_x}{J}\right)+\frac{\partial}{\partial\eta}\left(\frac{f_l\eta_x}{J}\right)+\frac{\partial}{\partial\zeta}\left(\frac{f_l\zeta_x}{J}\right)\right]+\frac{S_v}{J}=0, \tag{A8}$$

where coefficients Q_{11} to Q_{33} are defined as

$$\begin{aligned}
Q_{11}&=\xi_x^2+\xi_y^2+\xi_z^2,\\
Q_{12}&=Q_{21}=\xi_x\eta_x+\xi_y\eta_y+\xi_z\eta_z,\\
Q_{13}&=Q_{31}=\xi_x\zeta_x+\xi_y\zeta_y+\xi_z\zeta_z,\\
Q_{22}&=\eta_x^2+\eta_y^2+\eta_z^2,\\
Q_{23}&=Q_{32}=\eta_x\zeta_x+\eta_y\zeta_y+\eta_z\zeta_z,\\
Q_{33}&=\zeta_x^2+\zeta_y^2+\zeta_z^2.
\end{aligned} \tag{A9}$$

Since the x and y directions in the physical domain are identical to the ξ and η directions in the computational domain, respectively, the following relationships are obtained:

$$\begin{aligned}
x_\xi&=\frac{\partial x}{\partial\xi}=1;\quad x_\eta=\frac{\partial x}{\partial\eta}=0;\quad x_\zeta=\frac{\partial x}{\partial\zeta}=0,\\
y_\eta&=\frac{\partial y}{\partial\eta}=1;\quad y_\xi=\frac{\partial y}{\partial\xi}=0;\quad y_\zeta=\frac{\partial y}{\partial\zeta}=0.
\end{aligned} \tag{A10}$$

Using Eq. (A10), Eqs. (A2) and (A3) are simplified as

$$\begin{bmatrix}\xi_x & \xi_y & \xi_z\\ \eta_x & \eta_y & \eta_z\\ \zeta_x & \zeta_y & \zeta_z\end{bmatrix}=\begin{bmatrix}1 & 0 & 0\\ 0 & 1 & 0\\ -Jz_\xi & -Jz_\eta & J\end{bmatrix}, \tag{A11}$$

$$J=\frac{1}{z_\zeta}. \tag{A12}$$

Using Eqs. (A11) and (A12), the simplified version of the energy conservation equation in the curvilinear coordinate system, i.e., Eq. (3), is obtained.

B. Droplet characteristics during gas–metal arc welding

1. Droplet transfer frequency and radius

Rhee[33] and Jones[34] found that the droplet frequency was strongly affected by the welding current under the conditions of this investigation. In this study, the droplet transfer frequency is calculated by fitting their experimental results into a sigmoid function combined with a quadratic function, as shown in Fig. 12(a). The resulting equation is given as

$$f=\frac{-243.44}{1+\exp\left(\dfrac{I-291.086}{6.064\,37}\right)}+323.506-0.874\times I+0.0025\times I^2\ \ (\mathrm{Hz}), \tag{B1}$$

where I is the weld current in Ampere.

With the knowledge of the droplet transfer frequency, assuming that the droplets are spherical, the droplet radius r_d is given by

$$r_d=\sqrt[3]{\frac{3}{4}r_w^2 w_f\Big/ f}. \tag{B2}$$

2. Droplet impingement velocity

The molten droplets detached from electrode wire are accelerated in the arc column mainly by gravity and plasma drag force. If a constant acceleration is assumed, the velocity of droplets impinging the weld pool is given as

$$v_d=\sqrt{v_0^2+2a_dL_a}, \tag{B3}$$

where v_0 is the initial droplet velocity, a_d is the droplet acceleration, and L_a is the arc length. As shown in Eq. (B3), the knowledge of v_0, a_d, and L_a is required to calculate the droplet impingement velocity. The initial velocity of the droplets is estimated by fitting the experimental results of Lin *et al.*[35] in the following equation:

$$v_0=\sqrt{-0.336\,92+0.00\,854(I/D_d)}. \tag{B4}$$

The droplet acceleration, a_d, due to the plasma drag force and gravity is expressed as

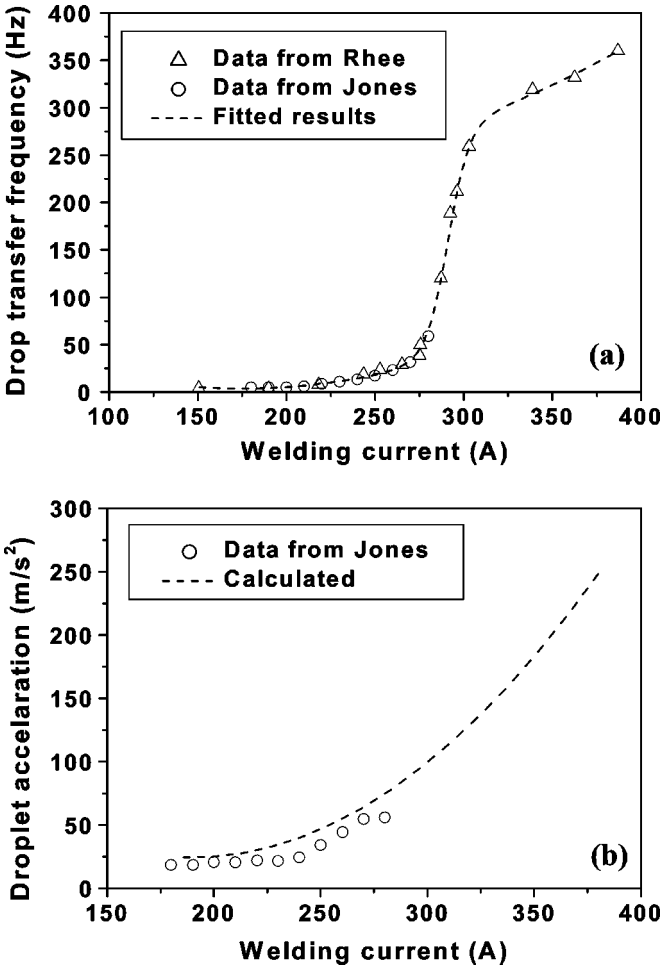

FIG. 12. Calculated droplet characteristics: (a) Comparison between the fitted and measured droplet transfer frequency and (b) comparison between calculated and measured droplet acceleration in the arc column.

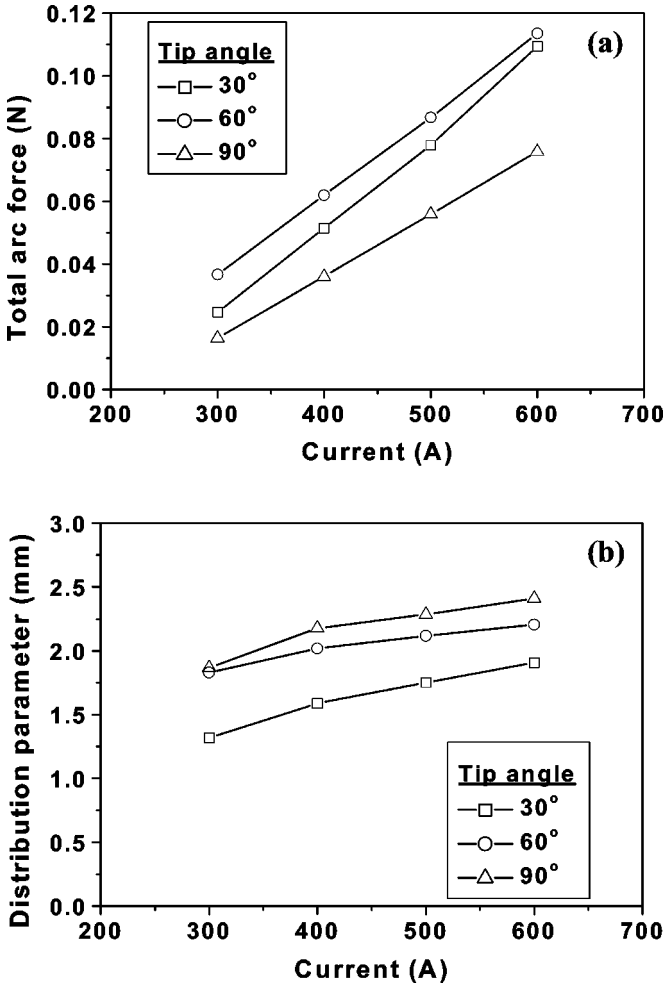

FIG. 13. Arc pressure distribution for three different tip angles: (a) calculated total arc force and (b) calculated pressure distribution parameter using a Gaussian function fitting.

$$a_d=\frac{3}{8}\frac{v_g^2\rho_g}{r_d\rho_m}C_d+g, \tag{B5}$$

where v_g and ρ_g are the velocity and density of argon plasma, respectively, r_d is the radius of droplet, C_d is the drag coefficient, ρ_m is the density of droplet, and g is the gravitational constant. The velocity of argon plasma is calculated using the following equation:[26]

$$v_g=k_1\times I, \tag{B6}$$

where k_1 is a constant and a value of 1/4 is used in this study. The other parameters in Eq. (B5) were calculated using the relationship and data available in Ref. 26. As shown in Fig. 12(b), the acceleration calculated using Eq. (B5) is in a good agreement with the corresponding experimental data.[34]

The arc length was estimated using the equivalent circuit of GMA welding system. In a steady state, the arc length is given by the following circuit equation:[36]

$$V_{\mathrm{OC}}=V_{a0}+(R_S+R_P+R_e+R_a)I+(E_{al}+E_{ai}I)L_a, \tag{B7}$$

where V_{OC} is the open-circuit voltage, R_S+R_P are the electrical resistance of the welding power source and cable, R_e is the electrical resistance over the electrode extension, V_{a0}, R_a, E_{al}, and E_{ai} are coefficients used in Ayrton's equation.[36] These parameters were determined from the data available in literature.[36]

In summary, the impingement velocity is calculated using Eq. (B3) with the estimated droplet initial velocity, acceleration, and arc length. The droplet impingement velocity, transfer frequency, and radius are then used to calculate the dimensions of the cylindrical volumetric heat source, as discussed in Sec. II C of the text.

C. Arc pressure distribution

The arc pressure P_a is normally approximated by a Gaussian distribution as[28,29]

$$P_a=\frac{F}{2\pi\sigma_p^2}\exp\left(-\frac{r^2}{2\sigma_p^2}\right), \tag{C1}$$

where F is the total arc force, σ_P is the arc pressure distribution parameter, and r is the distance from the axis of arc. In this study, the relationship of F and σ_P as a function of current was extracted from the experimental data of Lin and Eagar.[28] In their experiments, the arc pressure distribution was measured for tungsten electrodes with three different tip

angles (30°, 60°, and 90°). The total arc force is calculated by integrating the measured arc pressure distribution (P'_a):

$$F = \int 2\pi r P'_a dr. \tag{C2}$$

Once the total arc force is obtained, the pressure distribution parameter is determined by fitting the experimental distribution into Eq. (C1). Both the total force, F, and the distribution parameter, σ_P, are strongly affected by the welding current.[28] The calculated results for the total arc force and the pressure distribution parameter as a function of current are shown in Figs. 13(a) and 13(b), respectively. The fitted results for 60° tip angle are used in the present calculation.

[1] S. A. David and T. DebRoy, Science **257**, 497 (1992).
[2] T. DebRoy and S. A. David, Rev. Mod. Phys. **67**, 85 (1995).
[3] H. Zhao, D. R. White, and T. DebRoy, Int. Mater. Rev. **44**, 238 (1999).
[4] K. Mundra, T. DebRoy, and K. M. Kelkar, Numer. Heat Transfer, Part A **29**, 115 (1996).
[5] C. S. Wu and L. Dorn, Comput. Mater. Sci. **2**, 341 (1994).
[6] Z. N. Cao and P. Dong, J. Eng. Mater. Technol. (Trans ASME) **120**, 313 (1998).
[7] W. Zhang, G. G. Roy, J. W. Elmer, and T. DebRoy, J. Appl. Phys. **93**, 3022 (2003).
[8] W. Zhang, J. W. Elmer, and T. DebRoy, Mater. Sci. Eng., A **333**, 320 (2002).
[9] T. Cool and H. K. D. H. Bhadeshia, Sci. Technol. Weld. Joining **2**, 36 (1997).
[10] Z. Yang, J. W. Elmer, J. Wong, and T. DebRoy, Weld. J. (Miami) **79**, 97s (2000).
[11] Z. Yang, S. Sista, J. W. Elmer, and T. DebRoy, Acta Mater. **48**, 4813 (2000).
[12] T. Hong, W. Pitscheneder, and T. DebRoy, Sci. Technol. Weld. Joining **3**, 33 (1998).
[13] M. A. Quintana, J. McLane, S. S. Babu, and S. A. David, Weld. J. (Miami) **80**, 98s (2001).
[14] T. Hong and T. DebRoy, Ironmaking Steelmaking **28**, 450 (2001).
[15] K. Mundra, J. M. Blackburn, and T. DebRoy, Sci. Technol. Weld. Joining **2**, 174 (1997).
[16] H. Zhao and T. DebRoy, Metall. Mater. Trans. B **32B**, 163 (2001).
[17] T. A. Palmer and T. DebRoy, Metall. Mater. Trans. B **31B**, 1371 (2000).
[18] J.-W. Kim and S.-J. Na, Weld. J. (Miami) **74**, 141s (1995).
[19] H. G. Fan and R. Kovacevic, J. Phys. D **31**, 2929 (1998).
[20] S. Kumar and S. C. Bhaduri, Metall. Mater. Trans. B **25B**, 435 (1994).
[21] S.-K. Jeong and H.-S. Cho, Proc. Inst. Mech. Eng. **211B**, 63 (1997).
[22] S.-H. Cho and J.-W. Kim, Sci. Technol. Weld. Joining **6**, 220 (2001).
[23] G. Jelmorini, G. W. Tichelaar, and G. J. P. M. Van den Heuvel, *IIW Document 212-411-77* (International Institute of Welding, London, 1977).
[24] W. Zhang and T. DebRoy, *Proceedings of Mathematical Modeling and Information Technologies in Welding and Related Processes*, Crimea, Ukraine, edited by V. I. Makhnenko (E. O. Paton Electric Welding Institute. Kiev. Ukraine, 2002), p. 24.
[25] J. F. Thompson, Z. U. A. Warsi, and C. Wayne Mastin, *Numerical Grid Generation: Fundamentals and Applications* (Elsevier Science, New York, 1985).
[26] J. F. Lancaster, *The Physics of Welding*, 2nd ed. (Pergamon, Oxford, 1986).
[27] Z. Yang and T. DebRoy, Metall. Mater. Trans. B **30B**, 483 (1999).
[28] M. L. Lin and T. W. Eagar, Metall. Mater. Trans. B **17B**, 601 (1986).
[29] Y. S. Kim and T. W. Eagar, Weld. J. (Miami) **70**, 20s (1991).
[30] S. V. Patankar, *Numerical Heat Transfer and Fluid Flow* (McGraw–Hill, New York, 1982).
[31] K. Masubuchi, *Analysis of Welded Structures* (Pergamon, Oxford, 1980).
[32] K. A. Hoffmann and S. T. Chiang, *Computational Fluid Dynamics for Engineers* (Engineering Education System, Wichita, KS, 1993), Vol. 2.
[33] S. Rhee and E. Kannatey-Asibu, Jr., Weld. J. (Miami) **71**, 381s (1992).
[34] L. A. Jones, T. W. Eagar, and J. H. Lang, J. Phys. D **31**, 107 (1998).
[35] Q. Lin, X. Li, and S. W. Simpson, J. Phys. D **34**, 347 (2001).
[36] C.-H. Kim and S.-J. Na, Proc. Inst. Mech. Eng. **215B**, 1270 (2001).